

# High-order strong-coupling expansion for the Bose-Hubbard model

Tao Wang,<sup>1,2</sup> Xue-Feng Zhang,<sup>2,3,4,5,\*</sup> Chun-Feng Hou,<sup>6</sup> Sebastian Eggert,<sup>2</sup> and Axel Pelster<sup>2</sup>

<sup>1</sup>*School of Science, Wuhan Institute of Technology, 438000 Wuhan, China*

<sup>2</sup>*Physics Department and Research Center OPTIMAS,*

*Technical University of Kaiserslautern, 67663 Kaiserslautern, Germany*

<sup>3</sup>*Department of Physics, Chongqing University, Chongqing 401331, People's Republic of China*

<sup>4</sup>*Max-Planck-Institut für Physik komplexer Systeme,*

*Nöthnitzer Strasse 38, 01187 Dresden, Germany*

<sup>5</sup>*State Key Laboratory of Theoretical Physics, Institute of Theoretical Physics,  
Chinese Academy of Sciences, Beijing 100190, China*

<sup>6</sup>*Department of Physics, Harbin Institute of Technology, Harbin 150001, China*

Based on the process-chain method, we work out in detail a high-order strong-coupling expansion (HSCE) algorithm for determining the quantum phase boundary between the Mott insulator and the superfluid phase of the Bose-Hubbard model in different dimensions. A comparison with quantum Monte-Carlo results reveals the high efficiency and accuracy of the HSCE. With a symbolized evaluation of the algorithm we obtain an analytic expression for the strong-coupling boundary for different fillings up to eighth order. A subsequent Padé approximation then yields a scaling function, which rescales lobes with different fillings to one lobe. As a further crosscheck, we perform a hopping expansion of the phase boundaries obtained from the effective potential Landau theory (EPLT) and find that the respective expansion coefficients coincide with those of HSCE.

PACS numbers: 64.70.Tg, 73.43.Nq, 11.15.Me

## I. INTRODUCTION

In recent decades, strongly correlated systems play a crucial role in condensed matter physics. For high-temperature superconductors,<sup>1</sup> the on-site interaction between fermions becomes dominant in comparison with hopping processes. Thus, considering the hopping term as a perturbation, the Hubbard model can be reduced to the  $t - J$  model or the Heisenberg model at half filling. The bosonic counterpart is the Bose-Hubbard model,<sup>2</sup> which has been extensively studied theoretically and can be realized experimentally using a gas of bosonic atoms in optical lattices.<sup>3,4</sup> By reducing the tunneling processes via a deeper lattice potential or by using the Feshbach resonance technique, the interaction can be tuned in those systems, which allows the direct observation of a quantum phase transition from a superfluid to a Mott insulator phase.<sup>3,4</sup> But also dipolar molecules<sup>5</sup> or Rydberg atoms<sup>6</sup> can be loaded into an optical lattice, so that the strong long-range and anisotropic dipolar interaction plays a major role. In contrast to the weakly interacting case, strongly dipolar correlated systems exhibit many exotic phases, such as supersolid,<sup>7-9</sup> superradiant,<sup>10</sup> or other topological phases.<sup>11</sup>

In this paper we determine the phase boundary of the Mott-superfluid phase transition to high accuracy in the Bose-Hubbard model<sup>2</sup>

$$H = -t \sum_{\langle ij \rangle} (\hat{b}_i^\dagger \hat{b}_j + \hat{b}_j^\dagger \hat{b}_i) + \sum_i \left[ \frac{U}{2} \hat{n}_i (\hat{n}_i - 1) - \mu \hat{n}_i \right], \quad (1)$$

where  $\langle ij \rangle$  represents a sum over nearest-neighbor sites,  $t$  denotes the hopping matrix element,  $\hat{b}_i^\dagger (\hat{b}_i)$  creates (annihilates) a particle on site  $i$ ,  $U$  stands for the on-site

repulsion, and  $\mu$  is the chemical potential. The phase transition was first established using mean field theory,<sup>2</sup> but as we will show here it is possible to obtain very accurate results by obtaining high orders using a strong-coupling expansion (SCE) method, which was proposed by Freericks and Monien some time ago.<sup>12</sup> The strong-coupling ground state is given in the particle number representation, while the hopping term is treated as a perturbation, so that the energy of both the Mott insulator and a single particle (or hole) excited state can be calculated perturbatively. By equating the respective energies, the critical line between the Mott insulator and the superfluid phase can be deduced. In comparison with the mean-field approach,<sup>2</sup> this strong-coupling expansion method shows a higher accuracy for lower spatial dimensions, especially after an extrapolation to higher orders. Therefore, SCE has been used successfully to study the Bose-glass phase in the superlattice,<sup>13</sup> two-species bosons loaded into  $d$ -dimensional hypercubic optical lattices,<sup>14</sup> and the supersolid-solid quantum phase transition.<sup>15</sup> In particular, the strong-coupling expansion method has turned out to be efficient for the second-order transition from an incompressible to a compressible phase. However, the calculational efforts turn out to increase with the order in form of a power law, so analytic SCE is usually limited up to the fourth order. In order to obtain higher orders than 10 Eckardt et al. developed a computer assisted process-chain algorithm (PCA)<sup>16,17</sup> based on Kato's formulation of the perturbation calculus.<sup>18</sup> Using the PCA, high-precision results were obtained for both the ground-state energy and the correlation function within the Mott insulator.<sup>17</sup> Furthermore, by implementing PCA for the effective potential Landau theory (EPLT),<sup>19,20</sup> the critical line of the quantum phase tran-

sition from the Mott insulator to the superfluid phase was determined with high precision<sup>17,21</sup> so that even the corresponding critical exponents can be extracted.<sup>22</sup> In order to deal with degenerate states, such as particle-hole excitations, the PCA must be modified, which was shown by Heil and Linden for a one-dimensional (1D) system.<sup>23</sup> An alternative SCE approach by Elstner and Monien also obtained high-order results which can be applied to low dimensions and low filling.<sup>24</sup>

In this paper, we present the high-order SCE algorithm combined with the PCA for degenerate states in great detail, which is used to obtain *analytical* expressions up to eighth order on 1D, square (2D), and cubic (3D) lattices for arbitrary filling  $n$ . In Sec. II, we briefly review the strong-coupling expansion, for which we propose an efficient calculational method. Then, in Sec. III, we explain the high-order strong-coupling expansion (HSCE) algorithm in detail and apply it in Sec. IV to study the Bose-Hubbard model. The phase boundaries are calculated in 1D, 2D, and 3D for different filling and compared with high-precision quantum Monte Carlo (QMC) simulations. In Sec. V, we obtain the critical line for arbitrary fillings up to 10th order and determine their scaling properties, so that the lobes of different fillings can be rescaled to the infinite filling lobe. Additionally, in Sec. VI, we show that the HSCE results coincide with a hopping expansion of the high-order effective potential Landau theory (HEPLT). Finally, we draw our conclusions in Sec. VII.

## II. NOVEL STRONG-COUPLING EXPANSION METHOD

The strong-coupling expansion method is based on perturbation theory. It can be used to determine the second-order critical line of the incompressible phase, whose melting is caused by particle or hole excitations. Based on the work of Freericks and Monien,<sup>12</sup> one determines at first the unperturbed ground-state wave function of both the incompressible state and the particle (hole) excited state. Then one calculates the respective ground-state energies in terms of a hopping expansion by applying non-degenerate and degenerate perturbation theory. At last, by comparing the resulting ground-state energies, the corresponding critical line is deduced.

Let us take the second-order phase transition of a Mott insulator as a concrete example, which is described by the Bose-Hubbard model in Eq. (1). The dominant part is provided by the on-site repulsive interaction together with the chemical potential, i.e.  $H_0 = \frac{U}{2} \sum_i \hat{n}_i(\hat{n}_i - 1) - \mu \sum_i \hat{n}_i$ , whereas the perturbative part is the hopping term:  $H' = -t \sum_{\langle ij \rangle} (\hat{b}_i^\dagger \hat{b}_j + \hat{b}_j^\dagger \hat{b}_i)$ . When the tunnel matrix element  $t$  vanishes, the ground state of the Mott insulator with filling  $n$  is non-degenerate and uniquely given by  $\psi_M^{(0)} = \prod_i (\hat{b}_i^\dagger)^n |0\rangle / \sqrt{n!}$ . In contrast to that, the particle excited state  $\hat{b}_j^\dagger \psi_M^{(0)}$  is degenerate for

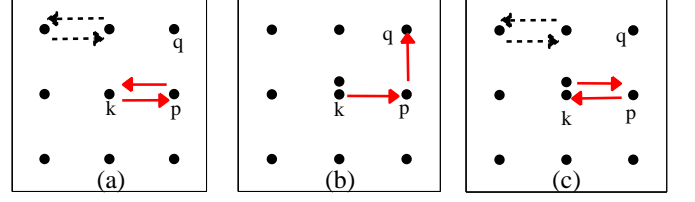


FIG. 1: Second-order arrow diagrams for (a) the ground state of a Mott insulator of filling one, and also for (b) open and (c) closed arrow diagrams for the case of adding one particle. As all arrow diagrams irrelevant to site  $k$ , indicated by black dashed arrows, cancel each other, only the arrow diagrams relevant to site  $k$ , highlighted by red solid arrows, need to be considered.

$t = 0$ , since no matter at which site the additional particle is located, the corresponding ground-state energies coincide.

The ground-state energy of the Mott insulator reads in zeroth order of the tunnel matrix element  $E_M^{(0)} = [Un(n-1)/2 - \mu n]N$ , where  $N$  denotes the number of sites. The first-order ground-state energy correction is zero, so the first non-vanishing correction is of second-order and follows from  $E_M^{(2)} = \sum_{i \neq 0} \langle \psi_M^{(0)} | H' | e_i \rangle \langle e_i | H' | \psi_M^{(0)} \rangle / (E^{(0)} - E_i)$ , where  $e_i$  denotes an excited state with energy  $E_i$ . According to Fig. 1 (a), the second-order processes correspond to the case that each particle is hopping to the nearest neighbor site and then back. Thus, the second-order perturbation energy yields  $E_M^{(2)} = -z(n+1)Nt^2/U$  where  $z = 2d$  stands for the coordination number in  $d$  dimensions. Then the ground-state energy of the Mott insulator up to second order in the tunnel matrix element is given by  $E_M = E^{(0)} - z(n+1)Nt^2/U$ .

For the particle excited state, the zeroth-order ground-state energy is given by  $E_p^{(0)} = E_M^{(0)} - \mu + nU$ . The general form of the ground state wave function is given by the superposition  $\psi_p^{(0)} = \sum_j a_j \hat{b}_j^\dagger \psi_M^{(0)}$  with the normalization constraint  $\sum_j |a_j|^2 = 1$ . The first-order ground-state energy is then determined via  $E_p^{(1)} = \langle \psi_p^{(0)} | H' | \psi_p^{(0)} \rangle$ . In order to minimize  $E_p^{(1)}$ , we need to diagonalize the matrix  $M_{i,j} = \psi_M^{(0)} \hat{b}_i H' \hat{b}_j^\dagger \psi_M^{(0)}$  and take the lowest eigenvalue as the resulting first-order ground-state energy. Thus, in other words, first-order perturbation lifts the degeneracy. Based on the underlying translational symmetry of the ground state, we obtain the first-order ground-state energy  $E_p^{(1)} = -z(n+1)t$  and the non-degenerate ground state turns out to be  $\psi_p^{(0)} = \sum_j \hat{b}_j^\dagger \psi_0 / \sqrt{Nn}$ . Now we turn to second-order processes, where Fig. 1(b) and (c) depict via red solid arrow diagrams the two possible types, which occur in the presence of one additional particle. The first diagram is an open diagram, which is characterized by  $|211\rangle \rightarrow |202\rangle \rightarrow |112\rangle$  with  $|n_k n_p n_q\rangle$  denoting the occupation of the sites  $k, p, q$  and has the corresponding energy  $-(n+1)t^2/U$ . The

second one is the closed diagram  $|21\rangle \rightarrow |30\rangle \rightarrow |21\rangle$  with  $|n_k n_p\rangle$  representing the occupation of the sites  $k$ ,  $p$  and the related energy  $-(n+2)t^2/(2U)$ . Note that the open diagram Fig. 1(b) has the multiplicity  $z(z-1)$ , whereas the multiplicity of the closed one in Fig. 1(c) is  $z$ . Besides that, we have to take into account in Fig. 1(b) and (c) that there are additional  $z(N-2)$  closed diagrams, indicated by black dashed arrow diagrams, which are not related to the additional particle. Thus, the second-order ground-state energy results in  $E_p^{(2)} = -[z(N-2)(n+1) + z(n+2)/2 + z(z-1)(n+1)]t^2/U$  and the total energy of the particle excited state is given by  $E_p = E_M^{(0)} - \mu + nU - z(n+1)t + E_p^{(2)}$ . Finally, equating the Mott and the particle excited ground-state energy according to  $E_M = E_p$ , we get the following critical line up to second order in the tunnel matrix element  $t$ :  $\mu_p = nU - z(n+1)t - [z(n+2)/2 + z(z-1)(n+1) - 2z(n+1)]t^2/U$ .

However, the number of arrow diagrams is of the order of the lattice size  $N$ , so this calculation is not practical in the thermodynamic limit even with the process-chain approach. Therefore, we introduce here a novel strong-coupling method, which turns out to be more practical and efficient as it is quite suitable for a computer implementation. From the above derivation of the second-order result for the critical line, we read off that perturbative calculations follow more easily from neglecting all energy contributions, which are not related to the site  $k$ , where the additional particle is located, as all those contributions irrelevant to site  $k$  in  $E_M$  and  $E_p$  cancel with each other at the end. Thus, in order to obtain the critical line to higher orders in the tunnel matrix element, we need the following three steps:

(i) We calculate the energies of the diagrams related to the site  $k$  based on the ground state  $\psi_M^{(0)}$ , and name them *energy corrections*. To this end we only need to find all closed arrow diagrams related to site  $k$  and calculate the contribution for each diagram to the non-degenerate ground-state energy. In Fig. 1 (a), we have  $z$  hopping processes, where a particle at site  $k$  hops to a nearest neighbor site and then back, as well as  $z$  hopping processes, where a particle at a neighbor site hops to site  $k$  and back, thus the second-order energy correction results in  $-2z(n+1)t^2/U$ .

(ii) We only determine the energy, which is related to the additional particle, and name it *strong-coupling (SC) energy*. To this end we need to find all arrow diagrams related to site  $k$  and calculate the contribution of each diagram to the degenerate ground-state energy. In Fig. 1, diagram (b) and (c) have the multiplicity  $z$  and  $z(z-1)$ , respectively, thus the corresponding SC energies read  $-z(n+2)t^2/(2U)$  and  $-z(z-1)(n+1)t^2/U$ .

(iii) Equating the energy of processes (i) and (ii), we obtain the resulting SCE critical line.

Based on this strong-coupling expansion method, we only need to consider finite diagrams, combine their evaluation with the process-chain method, and then obtain their perturbative value. Note that for the case of the hole excitation, the calculations proceed similarly, except that

the arrows point then in the direction, where the hole moves.

### III. ALGORITHM OF HIGH-ORDER STRONG-COUPLING EXPANSION METHOD

When perturbation theory is used, the respective orders have to be calculated recursively. To this end one has to consider different types of hopping processes which contribute to the considered perturbative order of the ground-state energy. However, such an algorithm has two disadvantages. (a) High-order results are based on lower orders. (b) It is hard to automatically generate the relevant hopping processes. In order to overcome those problem, Eckardt suggested to use the Kato representation of perturbation theory<sup>16</sup> for producing the respective perturbative terms in each order via a process chain approach which generates and evaluates the respective diagrams systematically. In view of the high-order strong-coupling expansion, we also use similar strategies. In the following, we discuss the three parts how to implement the algorithm in detail and take the lower-order terms for the Bose-Hubbard model in a square lattice as illustrative examples.

#### A. Kato representation

Kato worked out a particular representation for the perturbative terms of perturbation theory.<sup>18</sup> Therein, the  $n$ th order contribution to the ground-state energy for a perturbation of the Hamiltonian  $H'$  is given by the trace

$$E^{(m)} = \text{Tr} \sum_{\{\alpha_\ell\}} S^{\alpha_1} H' S^{\alpha_2} H' \dots H' S^{\alpha_{m+1}}. \quad (2)$$

Here each term is characterized by a Kato trace list

$$\langle \alpha_1 \alpha_2 \dots \alpha_{m+1} \rangle, \quad (3)$$

where the integers  $\alpha_1, \dots, \alpha_{m+1}$  fulfill the condition

$$\sum_{\ell=1}^{m+1} \alpha_\ell = m - 1, \quad \alpha_\ell \geq 0. \quad (4)$$

Furthermore, the operators  $S^{\alpha_\ell}$  are defined via

$$S^{\alpha_\ell} = \begin{cases} -|g\rangle\langle g| & \text{if } \alpha_\ell = 0 \\ \frac{|e\rangle\langle e|}{(E_g^0 - E_e^0)^{\alpha_\ell}} & \text{if } \alpha_\ell \neq 0, \end{cases} \quad (5)$$

where  $|g\rangle, |e\rangle$  and  $E_g^0, E_e^0$  denote wave functions and energies of the ground state and the excited states, respectively. Thus, we read off from Eq. (5) the relation

$$S^{\alpha_i} S^{\alpha_j} = \begin{cases} -S^0 & \alpha_i = \alpha_j = 0 \\ 0 & \alpha_i = 0, \alpha_j \neq 0 \text{ or } \alpha_i \neq 0, \alpha_j = 0 \\ S^{\alpha_i + \alpha_j} & \alpha_i \neq 0, \alpha_j \neq 0 \end{cases} \quad (6)$$

which is useful for simplifying products of operators  $S^{\alpha_\ell}$ . Additionally, we can conclude from Eq. (4) that there are at least two numbers in the Kato trace list  $\langle \alpha_1 \alpha_2 \dots \alpha_{m+1} \rangle$  which are zero. The goal is to use Eq. (6) and the cyclic permutation of operators under the trace to move the  $S^0$ -operators to the outside of the trace, so the expression can be rewritten in general as

$$\langle g | H' S^{\alpha'_1} H' \dots S^{\alpha'_{m-1}} H' | g \rangle. \quad (7)$$

If  $\alpha_1 = \alpha_{m+1} = 0$  we immediately obtain the new indices  $\alpha'_j = \alpha_{j+1}$ . If  $\alpha_1 \neq \alpha_{m+1} = 0$  or  $\alpha_1 \neq \alpha_{m+1} = 0$  the expression vanishes according to Eq. (6), so this case does not need to be considered. Finally, if  $\alpha_1 \neq 0$  and  $\alpha_{m+1} \neq 0$  cyclic permutations are used until  $S^0 = -S^0 S^0$  appears first in the product under the trace, which can then again be written in the form of Eq. (7) with a negative sign and one of the new indices with value  $\alpha_1 + \alpha_{m+1}$ . We define the resulting reduced list of indices as a *Kato-list* and use the abbreviated representation

$$(\alpha'_1 \alpha'_2 \dots \alpha'_{m-1}). \quad (8)$$

So far two ways have been used to calculate the Kato-lists. One was suggested by Eckardt<sup>16</sup> and can be realized by the following steps. At first we substitute the operator  $S^0$  with  $-|g\rangle\langle g|$  into the Kato-list and use the

abbreviation  $|g\rangle \rightarrow )$  and  $\langle g| \rightarrow ($ . With this the Kato-list changes into an array of elementary matrix element (EME) denoted by  $(\dots)$ , in which the operator  $S^0$  no longer exists. Note that the EME has the reflection symmetry, so we have for instance  $(\alpha_1 \alpha_2 \alpha_3) = (\alpha_3 \alpha_2 \alpha_1)$ . For convenience reasons we always change the form of the EME such that we take the smaller one, e.g. we use  $(121321)$  and not  $(123121)$ . After that, to order the array of EMEs, we define the relative value of the EME with the following two rules. (i) The numbers  $\alpha$  of the operators  $S^\alpha$  in the EME are firstly compared, thus we have  $(111) > (12)$ . (ii) When the numbers coincide, then we compare the integer  $\alpha$  of the first non-equal operator  $S^\alpha$ , so we have  $(123) < (132)$ . Along these lines we can order the EMEs in the Kato-list. As an example<sup>16</sup> starting with  $\langle 2021011001 \rangle$  can be transformed into the Kato-list  $-(11003021)$ . The resulting EMEs  $(11)(3)(21)$  can be ordered to obtain  $(3)(11)(12)$ . This result is then stored as a Kato-list  $-(03011012)$ . At the end, the final Kato-lists can be ordered according to similar rules as the array of EMEs.

Let us take the fourth-order perturbative term as a concrete example to show how to generate the Kato-lists step by step and how to order them for later usage. It can be proved that the resulting fourth Kato representation coincides with the standard result of perturbation theory.

Algorithm	Output
1. Generate all Kato trace lists for the considered order $n = 4$ .	$\langle 30000 \rangle, \langle 21000 \rangle, \langle 20100 \rangle, \dots, \langle 10101 \rangle, \dots, \langle 00003 \rangle$
2. Neglect all terms which have a zero at one end and are non-zero at the other end due to the second line of Eq. (6).	$\langle 03000 \rangle, \langle 02100 \rangle, \langle 02010 \rangle, \langle 00210 \rangle, \langle 01110 \rangle, \langle 00120 \rangle, \langle 01020 \rangle, \langle 01200 \rangle, \langle 00030 \rangle, \langle 10011 \rangle, \langle 10101 \rangle, \langle 11001 \rangle, \langle 20001 \rangle, \langle 10002 \rangle, \langle 00300 \rangle$
3. Change Kato trace list to Kato-list.	$(300), (210), (201), (021), (111), (012), (102), (120), (003), -(012), -(102), -(210), -(300), -(300), (030)$
4. Perform the substitutions $ g\rangle \rightarrow )$ and $\langle g  \rightarrow ($ and order array of EMEs.	$(())(3), -(())(12), -(1)(2), -(())(12), (111), -(())(12), -(1)(2), -(())(12), (())(3), (1)(2), (1)(2), (1)(2), -(())(3), -(())(3), (1)(3)$
5. Collect same arrays and determine their weight.	$-(1)(2), -2(1)(2), (1)(3), (111)$
6. Order and change them back to Kato-list.	$(003), 2(012), (102), (111)$

The advantage of this algorithm is that one can get for each order the smallest number of Kato-lists, so that the computation time is drastically reduced. But the Kato-lists following from the above algorithm are only suitable provided that the ground state is non-degenerate. Let us illustrate this by the process  $\langle g_1 | H' S^{\alpha'_1} H' | g_2 \rangle \langle g_2 | H' S^{\alpha'_2} H' | g_3 \rangle$ , which involves the three degenerate ground states  $|g_1\rangle, |g_2\rangle, |g_3\rangle$  and can be represented by the Kato-list  $(\alpha'_1 0 \alpha'_2)$ . If we transform the Kato-list into EMEs and change their order, the calculation process may be changed to  $\langle g_2 | H' S^{\alpha'_1} H' | g_3 \rangle \langle g_1 | H' S^{\alpha'_2} H' | g_2 \rangle$ . But this cannot be

mapped back to the Kato-list  $(\alpha'_2 0 \alpha'_1)$  as the number 0 in the Kato-list corresponds to  $\sum_j |g_j\rangle\langle g_j|$ , but not  $\sum_{i,j} |g_i\rangle\langle g_j|$ .

A second approach for calculating Kato-lists was proposed in Ref. [23] in order to also treat degenerate ground states, which was then applied to a 1D system. Here the Kato-lists (8) have to fulfill the conditions

$$\sum_{\ell=1}^{m-1} \alpha'_\ell = m-1, \quad \alpha'_\ell \geq 0 \quad (9)$$



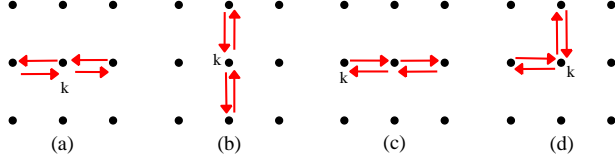


FIG. 2: Arrow diagrams of 4th order in the square lattice, which are topologically equivalent

and

$$\sum_{\ell=1}^s \alpha'_\ell \leq s, \quad \text{for } s = 1, \dots, m-2. \quad (10)$$

Thus, more Kato-lists appear in each order, so the computational effort increases. In particular, now each Kato-list appears with the multiplicity one. For instance, in fourth order we no longer have the Kato-lists (003), 2(012), (102), (111) for a non-degenerate ground state but instead (003), (012), (021), (102), (111).

In conclusion, the original Kato-lists in Ref. [16] are useful for calculating non-degenerate ground-state energies as they show up, for instance, for Mott states. In contrast to this, the degenerate states of particle and hole excitations, as they appear within the strong-coupling method, have to be determined from Kato-lists of multiplicity one with restrictions in Eq. (9) and (10).<sup>23</sup>

### B. Arrow diagrams generalization

Whereas the determination of the underlying Kato-lists is independent of the considered system, we now turn to their diagrammatic representation, which does depend on the underlying Hamiltonian or the topology of the lattice. To this end we follow Refs. [16,23] and remark that an expression  $\langle e_1 | H' | e_2 \rangle$  in the Kato-list can be represented by an arrow. Thus, in a lattice system, each perturbative term can be graphically depicted as an arrow diagram. According to the linked cluster theorem, only connected diagrams contribute to the ground-state energy, thus we only need all non-equivalent connected arrow diagrams. Whereas for the calculation of the non-degenerate ground-state energy only closed connected diagrams appear, for degenerate ground-state energies also open connected diagrams have to be considered. For instance, for a particle (hole) excited degenerate ground state, each perturbative term is equivalent to the hopping of a particle (hole) to another site, so any open connected diagram has exactly two ends. Thus, the respective arrow diagram can be interpreted as the path of a walking particle.

In order to generate all non-equivalent arrow diagrams, we fix at first the starting point at the center, and use different numbers or characters to label the respective directions. For instance, in case of a square lattice, we ab-

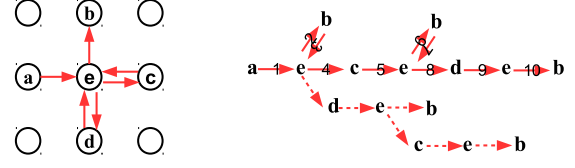


FIG. 3: One 6th-order arrow diagram labeled with (*rdurlu*) is shown in the left panel, its corresponding tree graph is shown in the right panel. Red solid arrows in the right panel are paths, which are passed due to the algorithm, and the dashed arrows represent other possible paths. The arrows (2, 3, 6, 7) indicate trace back process, so the smallest path is (1, 4, 5, 8, 9, 10). Thus, the smallest diagram representation is provided by (*rrlduu*).

breviate up as ‘*u*’, down as ‘*d*’, left as ‘*l*’, and right as ‘*r*’. After that, we get all possible connected arrow diagrams by applying combinatorics and represent them with the corresponding arrays of characters. Let us consider the second-order arrow diagrams as a concrete example: in case of a square lattice we have in total 16 diagrams, but only (*ud*), (*du*), (*lr*), and (*rl*) represent closed diagrams, whereas the others are open ones. Each diagram can have a non-unique representation, such as the 4th-order diagram Fig. 2(a), which can be represented by (*lrll*) or by (*rrll*). If we define the priority  $r < u < l < d$  and only take the smallest one according to this order. Therefore, the array corresponding to Fig. 2(a) is identified with (*rrll*). Proceeding in this way we avoid an overcounting of diagrams.

However, judging whether the diagram representation is the smallest one is not trivial, since there are several ways to follow a given set of arrows that point in and out from a central site as shown in Fig. 3. All possible paths can be drawn in form of a tree graph as shown in the right panel of Fig. 3. The smallest path, which passes through all the arrows, is the one to be determined. To this end, one can go through the whole diagram by moving in each step through the smallest arrow, but it is not allowed to move through one and the same arrow again. If one cannot finish with passing all the arrows, one has to trace back to the latest site, which has at least two arrows pointing out, and has now to choose the next smallest arrow to move through. After several tracing back processes, one gets the smallest diagram representation, when all arrows are passed.

After having produced all the smallest diagrams of the considered perturbative order, we reduce the number of diagrams due to symmetries and take the number of equivalent diagrams as its corresponding weight. For the lattice system, we can take into account both point group symmetry and translational symmetry. Taking again the square lattice as an example, its point symmetry  $D_4$  has 8 operations. For instance, diagram Fig. 2(b) can be ob-

tained by rotating Fig. 2(a) by 90 degrees to the right. After implementing all 8 operations on Fig. 2, we obtain only two different diagrams (a) and (b), so their weight is 2. Furthermore, for the Mott insulating state we can also consider the translational symmetry. The diagram Fig. 2(c) can be obtained by moving the diagram Fig. 2(a) one lattice site to the right. As the diagram Fig. 2(a) covers 3 sites, the total number of group operations is  $8 \times 3 = 24$ . After having performed all these operations on diagram Fig. 2(a), we find that there are in total six diagrams with the same contribution, so its weight is finally six. For the particle (hole) excited state, the starting point should always be at site  $k$ , so there is no translational symmetry and only the point group symmetry can be considered. Based on group theory, we find a more generic method to determine the weight of the smallest arrow diagram. To this end we denote the symmetry group by  $G$  and the number of its elements by  $n_G$ . If an arrow diagram is not changed under  $n_g$  group operations, this means that these operations belong to a subgroup  $g$  of  $G$  and that there are  $n_G/n_g$  different arrow diagrams. These arrow diagrams can be obtained by performing group operations on each other and they are not changed under operations, which belong to the subgroup  $g$ . The smallest arrow diagram can be stored and its weight turns out to be  $n_G/n_g$ . Note that, in contrast to calculating the ground-state energy of the Mott insulator, for particle (or hole) energy corrections, the weight does not need to be divided by the number of covered sites, since no overcounting exists. In Table I we show up to 12th perturbative order in the square lattice the number  $n_s$  of diagrams after having applied the reduction by symmetry. For energy corrections, we consider only closed diagrams with both point group and translational symmetries. But for the SC energy both closed and open diagrams appear, but a reduction occurs only due to point group symmetries. Consequently, although both energies contain closed diagrams, they have different weights due to the different symmetry considerations.

In addition to those symmetry considerations, we can further reduce the diagram number by considering their topology. As there is no long-range diagonal interaction and the on-site Hamiltonian  $H_0$  is uniform, the diagrams (d) and (a) of Fig. 2 have the same value. By marking the respective positions between different sites in the diagram and relabeling the involved site indices, we can find all topological equivalent arrow diagrams and store the smallest one at the end. Then, the sum of their weights is considered to be the new weight of the diagram. For the diagrams shown in Fig. 2, only (c) needs to be stored. From Table I, we find that the reduction due to topology dramatically decreases the number of diagrams  $n_t$ , especially for the open diagrams which represent the dominant part of the particle (or hole) energy. Moreover, note that for a bipartite lattice no closed diagram exists in any odd perturbative order.

Thus, the algorithm concerning the diagrammatic representation of Kato-lists is summarized as follows. At

$i$	Energy correction		SC energy	
	$n_s$	$n_t$	$n_s$	$n_t$
1	0	0	1	1
2	1	1	3	2
3	0	0	10	4
4	4	3	36	10
5	0	0	129	22
6	12	7	477	58
7	0	0	1784	140
8	75	29	6668	390
9	0	0	24909	988
10	510	121	92748	2815
11	0	0	344907	7412
12	4284	698	1278092	21516

TABLE I: Number of different connected arrow diagrams in square lattice for Mott energy correction and strong-coupling energy after reduction due to symmetries ( $n_s$ ) and topologies ( $n_t$ ).

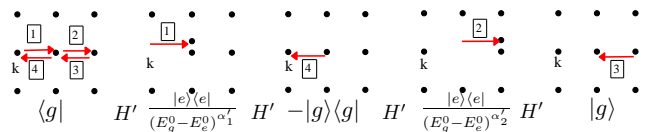


FIG. 4: One process chain of energy correction Kato-list with arrow order 1 4 2 3 matches Kato-list ( $\alpha'_1 0 \alpha'_2$ ).

first all connected arrow diagrams are produced by combinatorics, discarding the overcounted ones. Afterward, both symmetry and topology considerations reduce the number of different arrow diagrams.

### C. Calculation

At last, we turn to the explicit calculation of the energy corrections for the non-degenerate Mott state.<sup>16</sup> To this end one has to take into account that there are several ways for each arrow diagram to specify the arrow order and each order list is called a *process chain*. To illustrate this by a concrete example, we consider again the fourth-order diagram in the square lattice. Based on the arguments above, we only store in Fig. 2 the arrow diagram (c), which is characterized by  $(rrll)$ . If we label each arrow with a number, we have in total four processes. Taking into account all permutations, we have  $4! = 24$  types of process orders or process chains. In Fig. 4, we show one possible process chain with arrow order 1 4 2 3. All Kato-lists, which satisfy the form  $(\alpha'_1 0 \alpha'_2)$  with  $\alpha'_1 \neq 0, \alpha'_2 \neq 0$ , contribute to the respective energy correction. From Section III A we read off that only the Kato-list (102) appears. For the Mott insulator with filling  $n$ , the energy correction of this process chain is given



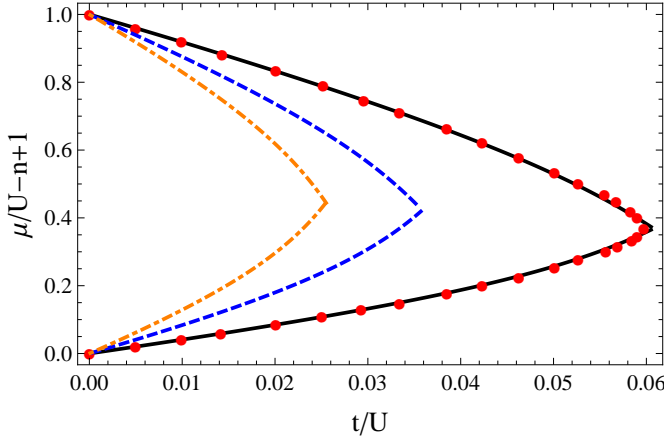


FIG. 7: Quantum phase diagram of 2d bosonic lattice system for  $n = 1$  (black solid line),  $n = 2$  (blue dot-dashed line), and  $n = 3$  (orange dashed line). For  $n = 1$  we also show QMC simulation results (red dot).<sup>31</sup>

in order to deal with the perturbative data.<sup>29,30</sup> To this end we follow the procedure outlined in Ref. [23] and perform at first a Borel transformation of the Eqs. (11), (12):

$$B(z) = \sum_{i=0}^{\infty} \beta^{(i)} \frac{z^i}{i!}, \quad (13)$$

where we have  $\beta^{(0)} = 1$  and  $\beta^{(0)} = 0$  for the particle and hole branch of the Mott lobe, respectively. Such a Borel transform is then rewritten and approximated according to Padé in order to capture the asymptotic behavior at the tip of the Mott lobe:

$$B(x) = \frac{\sum_{m=0}^{m_{\max}} a_m x^m}{1 + \sum_{n=1}^{n_{\max}} b_n x^n}. \quad (14)$$

Here we have for the upper boundary  $a_0 = 1$ , while  $a_0 = 0$  for the lower boundary. Afterward the final expression of the quantum phase boundary is recovered by evaluating the inverse Borel transformation via the integral

$$\mu(t) = \int_0^{\infty} B(xt) e^{-x} dx. \quad (15)$$

From the resulting phase diagram in Fig. 6 we read off that the one-dimensional system turns out to have similar lobe structures for different fillings. A quantitative comparison with extensive DMRG calculations<sup>26</sup> shows that our method reveals a quite high accuracy for the one-dimensional system. By implementing the Padé-approximation for different fillings  $n$ , we obtain the critical hopping amplitudes  $t_c/U = 0.265 \pm 0.01$  ( $n = 1$ ),  $t_c/U = 0.155 \pm 0.007$  ( $n = 2$ ), and  $t_c/U = 0.110 \pm 0.003$

$i$	$\beta_u^{(i)}$
1	12
2	45
3	666
4	47619/4
5	2445191/10
6	5195183971/1000
7	2738743631303/22500
8	21253373295304291/7560000
9	1114321983387473099/15876000
10	4247752706302638576591251/2500470000000

$i$	$\beta_d^{(i)}$
1	6
2	36
3	720
4	10932
5	260400
6	14700232/3
7	1150850656/9
8	24247779436/9
9	5917432656908/81
10	46545234375565613/28350

TABLE II: Different orders for HSCE coefficients of particle and hole critical line of the Mott lobe  $n = 1$  for the cubic lattice.

( $n = 3$ ). For the filling  $n = 1$  our finding lies within the error bars of the DMRG result for the critical point, which is given by  $t_c/U = 0.2776 \pm 0.01$ .<sup>26</sup>

In the square lattice system, where we have  $d = 2$ , we have also obtained a 10th order result for Eqs. (11) and (12), which goes beyond the 8th order result of Ref. [27]. But here we use a linear fit for extrapolating the strong-coupling results to infinite order. In particular, for a fixed value of the chemical potential  $\mu/U$  the strong-coupling critical hopping amplitude  $t_c/U$  is linearly fitted versus  $1/\text{order}$  to determine the infinite order critical hopping amplitude for both the upper and the lower boundaries. From the resulting quantum phase diagram in Fig. 7 we can see that our result agrees quite well with the QMC simulations of Ref. [31], except for a small discrepancy at the tip of the lobe. In particular, by extrapolating both  $\mu$  and  $t$ -values at the tip, we find for the critical hopping amplitudes  $t_c/U = 0.0597 \pm 0.002$  ( $n = 1$ ),  $t_c/U = 0.0349 \pm 0.003$  ( $n = 2$ ), and  $t_c/U = 0.0266 \pm 0.002$  ( $n = 3$ ) at the tip of the lobe. The corresponding QMC result for the critical hopping amplitude at filling  $n = 1$  reads  $t_c/U = 0.5974 \pm 0.0003$ .

At last we consider the cubic lattice, i.e. the case  $d = 3$ , where the strong-coupling result for the critical lines of the Mott lobes is so far only known up to third order from Ref. [12]. Therefore, we list explicitly the pertur-



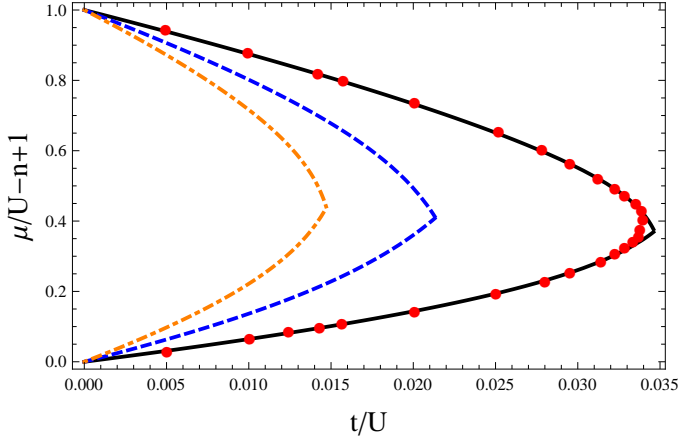


FIG. 8: Quantum phase diagram of 3d bosonic lattice system for  $n = 1$  (black solid line),  $n = 2$  (blue dot-dashed line), and  $n = 3$  (orange dashed line). For  $n = 1$  we also show QMC simulation results (red dots).<sup>32</sup>

bative coefficients in Eqs. (11) and (12) for  $n = 1$  up to the 10th order in Table II as reference data. From Fig. 8 we read off that our result deviates from QMC simulation results<sup>32</sup> around the lobe tip. This indicates that the 10th perturbative order considered here is not high enough for  $d = 3$ . Thus, the HSCE gives more accurate results for lower dimensions than for higher dimensions. Whereas the system becomes more classical in higher dimension, the strong-coupling expansion apparently takes quantum fluctuations better into account. Extrapolating the critical hopping amplitude for each order similar to the square lattice, we obtain for the tip of the lobes  $t_c/U = 0.03415 \pm 0.00004$  ( $n = 1$ ),  $t_c/U = 0.02012 \pm 0.00003$  ( $n = 2$ ), and  $t_c/U = 0.01430 \pm 0.00003$  ( $n = 3$ ). The corresponding QMC result<sup>32</sup> of the critical hopping amplitude for  $n = 1$  is  $t_c/U = 0.03408 \pm 0.00002$ , which is quite close to our result.

## V. SCALING PROPERTIES

In this section we investigate systematically the filling-dependent scaling properties of the Bose-Hubbard quantum phase diagram. To this end we have applied our HSCE method to determine the critical lines from Eqs. (11) and (12) of a general Mott lobe  $n$  also with symbolic calculations. The corresponding results are shown up to 8th order in Appendix A. In the following we do not consider the exceptional case of  $1d$ , as there the Mott insulator undergoes a BKT quantum phase transition to the superfluid phase, and restrict ourselves just to the 2d and the 3d system.

At first, we consider the scaling properties of the critical point  $t_c(n)$  for different filling  $n$ , which represents the tip of the Mott lobe. To this end we follow Ref. [33] and use the second-order strong-coupling result in order to re-express the hopping amplitude of the lobe tip for

large filling  $n$  according to

$$t_c(d, n)/U = \left( \frac{2d - \sqrt{-10d + 12d^2}}{(10 - 8d)d} \right) \times \left( 1 - \frac{1}{2n} + O\left[\frac{1}{n^2}\right] \right) \frac{1}{n}. \quad (16)$$

Thus, in the limit of large filling, the effects of dimension  $d$  and filling  $n$  turn out to decouple. Assuming that such a decoupling property also holds for higher strong-coupling orders, we perform for the critical hopping amplitude the ansatz

$$t_c(d, n)/U = f_t(d) \frac{g_t(n)}{n}, \quad (17)$$

where the filling-dependent factor represents a Taylor series in  $1/n$ :

$$g_t(n) = 1 + \sum_{i=1}^{\infty} \frac{a_i}{n^i}. \quad (18)$$

In the limit of infinite filling we then conclude

$$f_t(d) = \lim_{n \rightarrow \infty} n t_c(d, n)/U. \quad (19)$$

This means that  $f_t(d)$  can be calculated both for  $d = 2$  and  $d = 3$  from the term with highest filling number in each strong-coupling order for both the upper and the lower phase boundary presented in Appendix A. Note that in the limit of infinite filling the particle-hole symmetry is recovered because the Hamiltonian (1) does then not change with the transformation  $\hat{b}^\dagger \rightarrow \hat{b}'$ ,  $\hat{b} \rightarrow \hat{b}'^\dagger$ , which implies for the filling  $n \rightarrow n' + 1 \approx n'$ . This is reflected in the strong-coupling result for the quantum phase boundaries by the property that the coefficients of the highest filling in the upper and the lower branch have the same absolute value but a different sign.

After having obtained  $f_t(d)$  for  $d = 2$  and  $d = 3$ , we directly read off from Eq. (17) the filling-dependent function  $g_t(n) = n t_c(d, n)/[f_t(d)U]$  in each strong-coupling order. In order to approach the infinite-order case, we perform a Padé approximation and rewrite the filling-dependent function as

$$g_t(n) \approx \tilde{g}_t(n) = \frac{n^M + \sum_{i=0}^{M-1} \alpha_i n^i}{n^M + \sum_{j=0}^{M-1} \beta_j n^j}. \quad (20)$$

Here  $M$  is an integer, which characterizes the order of the Padé approximation. The resulting function  $\tilde{g}_t(n)$  represents the scaling function of the critical hopping amplitude. In Fig. 9 we have chosen  $M = 4$  and have used the critical hopping amplitude at the tip of the first 100 Mott lobes to fit the scaling function. In addition it turns out that the scaling functions in two and three dimensions

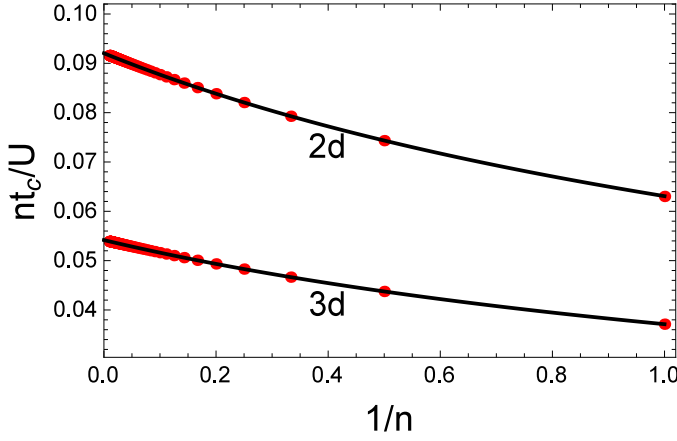


FIG. 9: Critical hopping amplitudes  $t_c$  for filling numbers  $n$  from 1 to 100 (red dots) compared with the value of  $f_t(d)$  times the scaling function  $g_t(n)$  (black line) in two and three dimensions.

nearly coincide, which supports the above assumption from Eq. (17) that dimension and filling decouple.

Furthermore, one can also use a similar strategy in order to investigate the scaling of the critical chemical potential  $\mu_c(d, n)/U$  at the lobe tip. But then the above mentioned particle-hole symmetry for infinite filling implies for the chemical  $\lim_{n \rightarrow \infty} \mu_p/U = 1 - \lim_{n \rightarrow \infty} \mu_h/U$ , so the critical chemical potential reads  $\lim_{n \rightarrow \infty} \mu_c/U = 1 - \lim_{n \rightarrow \infty} \mu_c/U = 1/2$ . Thus, the dimension dependent function is then given by  $f_\mu(d) = \lim_{n \rightarrow \infty} \mu_c/U = 1/2$  and the resulting scaling function  $g_\mu(d, n) = 2\mu'_c(d, n)/U$  with  $\mu'_c(d, n) = \mu_c(d, n)/U - n + 1$  has the Padé approximation

$$g_\mu(d, n) \approx \tilde{g}_\mu(d, n) = \frac{n^M + \sum_{i=0}^{M-1} \alpha'_i n^i}{n^M + \sum_{j=0}^{M-1} \beta'_j n^j}. \quad (21)$$

Note that, in contrast to the critical hopping, the scaling functions  $\tilde{g}_\mu(d, n)$  for the chemical potential turns out to have a residual dependence on the dimension  $d$ .

By assuming that the entire critical lines have the same scaling functions as the tips of the Mott lobes, we can map all Mott lobes for different filling numbers to the infinite filling lobe as follows. For each critical point  $\{\mu'(d, n), nt(d, n)/U\}$  in the lower branch of the Mott lobe, we define the rescaled value as  $\{\mu'_\infty, (tn)_\infty/U\} = \{\mu'(d, n)/\tilde{g}_\mu(n), t(d, n)n/[\tilde{g}_t(n)U]\}$  and, correspondingly, for each critical point in the upper branch we rescale according to  $\{\mu'_\infty, (tn)_\infty/U\} = \{1 - [1 - \mu'(d, n)]/[2 - \tilde{g}_\mu(n)], t(d, n)n/[\tilde{g}_t(n)U]\}$ . In Fig. 10 we observe that all scaled Mott lobes, obtained from different filling numbers, deviate only slightly from the quantum phase boundary at infinite filling.

Finally, we comment upon why the scaling property turns out to be more complicated for the one-dimensional

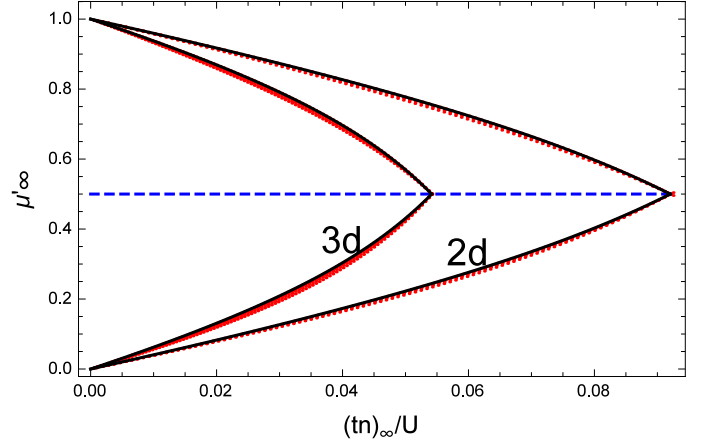


FIG. 10: Scaled Mott lobe obtained from different fillings  $n$  (red dots) compared with infinite filling quantum phase diagram (black line). For each dimension the scaled Mott lobes deduced from filling number  $n = 1, 2, 3, 4, 10, 100, 10000$  are almost on top of each other.

system. Although we could also find a scaling function for the critical point, this scaling function could not be used to map all the lobes to the infinite filling lobe. Whereas a Mott lobe with finite filling reveals a reentrant phenomenon due to the BKT quantum phase transition, this reentrance phenomenon disappears in the limit of an infinite filling due to the particle-hole symmetry between the upper and the lower phase boundary. Thus, in one dimension there does not exist a universal scaling function for all points of the quantum phase diagram.

## VI. COMPARISON WITH HIGH-ORDER EFFECTIVE POTENTIAL LANDAU THEORY

As has already been explained in the introduction, both SCE<sup>12</sup> and EPLT<sup>19,20</sup> represent two analytical perturbative methods for determining the quantum phase boundary of lattice systems. Usually the accuracy of their results are only compared in lower orders. Thus, in order to allow for a comparison in higher orders, we have also investigated the 2d Bose-Hubbard model with the HEPLT method from Ref. [17] up to 10th order. Whereas the HSCE method allows to determine the upper or the lower quantum phase boundary with one single calculation, HEPLT is more involved and needs independent calculations to obtain the critical hopping for each chemical potential. Note that, up to the same order, HSCE turns out to be faster than HEPLT because it has not to deal with additional source terms.

Comparing the accuracy of both methods in 10th order, we find that the effective potential result has an error of about 2.4 percent, while the strong-coupling result turns out to have an error of about 5.0 percent. Thus we conclude that HEPLT is more accurate than HSCE up to the same order. From Fig. 11 we also read off that

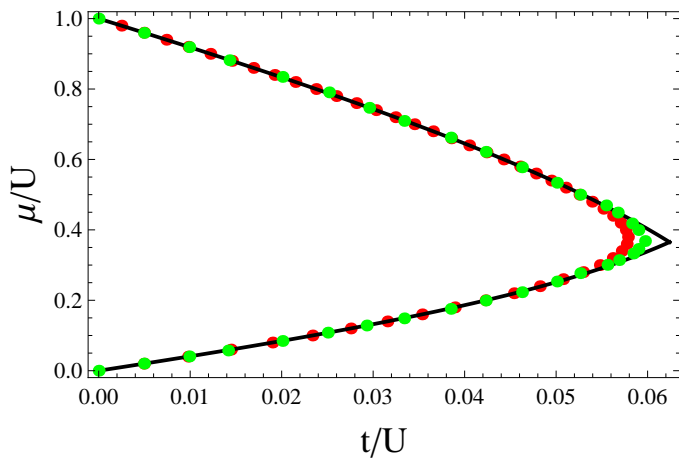


FIG. 11: Comparison of quantum phase diagrams for  $d = 2$  via HSCE (black line) and HEPLT (red dots)<sup>17</sup> in 10th order with QMC results (green dots)<sup>31</sup> at  $n = 1$ .

the HEPLT result always gives smaller hopping values than the QMC result, while the HSCE result gives larger values. Thus, we could use both methods in order to determine the region in the quantum phase diagram, where the phase boundary must exist. Extrapolating the results for both methods to infinite order yields quantum phase boundaries, which are basically indistinguishable from QMC<sup>31</sup> in the 2d system. However in 3d a comparison with results from QMC<sup>32</sup> reveals that extrapolating the 10th order of HSCE has the same accuracy as extrapolating the 8th order of HEPLT.<sup>17</sup> Thus, up to same order, the HEPLT method turns out to be more accurate in higher dimensional systems.

In a previous paper<sup>34</sup> we have pointed out the intriguing observation that, up to the second order, the SC coefficients coincide with those of a hopping expansion of the EPLT quantum phase boundary. Thus, for the Mott lobe  $n$ , one obtains the SC upper (lower) critical line by performing a hopping expansion of the EPLT quantum phase boundary around  $\mu/U = n - 1$  ( $\mu/U = n$ ). In view of proving such relations also for higher orders, we perform a symbolic calculation for the HEPLT method up to 8th order. By a corresponding hopping expansion of the HEPLT quantum phase boundary we obtain, indeed, the same coefficients of both the upper and the lower HSCE critical lines.

## VII. CONCLUSION

In this paper we have used the process-chain approach<sup>16,17</sup> for implementing the strong-coupling ex-

pansion method<sup>12</sup> to higher orders. To this end we have worked out our algorithm in sufficient detail, so that the respective steps should be reproducible for the reader. Further information is accessible in a Matlab code in the supplementary material,<sup>35</sup> which can also be downloaded from our homepage.<sup>36</sup> As a concrete example we have calculated for the Bose-Hubbard model the quantum phase diagram between the superfluid and the Mott insulator in different dimensions. A comparison with DMRG and Quantum Monte Carlo calculations from the literature has shown that our HSCE method is more suitable for lower dimensional systems.

Furthermore, we have performed symbolic calculations in order to obtain the critical lines for the Mott insulator-superfluid transition also for different fillings and dimensions. This has allowed us to investigate systematically the scaling properties of the quantum phase diagram. At the lobe tips we have found that the scaling functions of the critical hopping almost coincide for both two and three dimensions, while the corresponding scaling functions of the critical chemical potential turn out to be different. With these scalings at the lobe tip it is has then been possible to approximately map all the Mott lobes of different fillings to the infinite filling Mott lobe.

Finally, we have compared the HEPLT method from the literature with the HSCE method developed here and have concluded that the latter is easier to implement. However, it has also turned out that HSCE is not as accurate as HEPLT up to the same order. Furthermore, we have verified an intimate relation between both methods. It was verified that the phase boundaries from HEPLT and HSCE agree up to 8th order in a power series with respect to the hopping.

## Acknowledgments

We are thankful for useful discussions with A. Eckardt, C. Heil, and M. Holthaus. This work was supported by the "Allianz für Hochleistungsrechnen Rheinland-Pfalz", by the German Research Foundation (DFG) via the Collaborative Research Centers SFB/TR49 and SFB/TR185, as well as by the Chinese Academy of Sciences via the Open Project Program of the State Key Laboratory of Theoretical Physics. This work was also supported by the Startup Foundation for Introducing Talent of NUIST, No. 2015r060 and the Special Foundation for theoretical physics Research Program of China, No 11647165.

### Appendix A: Strong-coupling quantum phase boundary for arbitrary Mott lobe

Here we present our strong-coupling results for the critical lines in Eqs. (11) and (12) of the Bose-Hubbard quantum phase diagram for a general Mott lobe  $n$ , which were obtained with symbolic calculations up to the 8th order. At first, we consider the Bose-Hubbard chain, i.e. the case  $d = 1$ , where the upper boundary reads

$$\begin{aligned} \mu_p = & n - 2(n+1)t + n^2t^2 + (n^3 + 3n^2 + 2n)t^3 + \frac{1}{120}(221n^4 - 70n^3 - 559n^2 - 270n)t^4 + \frac{1}{3600}(11063n^5 \\ & + 56453n^4 + 127443n^3 + 114703n^2 + 32650n)t^5 + \frac{1}{9072000}(4201738n^6 - 159047706n^5 - 1019369927n^4 \\ & - 1684710576n^3 - 1075545275n^2 - 246900750n)t^6 + \frac{1}{11430720000}(65154949955n^7 + 852816554717n^6 \\ & + 4617015079493n^5 + 10042635987533n^4 + 10398278064548n^3 + 5217933284246n^2 + 1032937732500n)t^7 \\ & - \frac{1}{35012981203200000}(200810348470291303n^8 + 5778066670166672114n^7 + 43424519219943077927n^6 \\ & + 134818712387825712764n^5 + 207253111515652899680n^4 + 168130666829189484230n^3 \\ & + 69538136222775683026n^2 + 11689091525838787500n)t^8, \end{aligned} \quad (A1)$$

whereas the lower boundary is given by

$$\begin{aligned} \mu_h = & (n-1) + 2nt - (n^2 + 2n + 1)t^2 + (n - n^3)t^3 + \frac{1}{120}(-221n^4 - 954n^3 - 977n^2 - 246n - 2)t^4 + \frac{1}{3600} \\ & (-11063n^5 + 1138n^4 - 12261n^3 - 39538n^2 - 15076n)t^5 + \frac{1}{9072000}(-4201738n^6 - 184258134n^5 \\ & + 161105327n^4 + 718257312n^3 + 484129979n^2 + 107088822n + 54432)t^6 + \frac{1}{11430720000}(-65154949955n^7 \\ & + 396731905032n^6 - 868369700246n^5 - 2530614337602n^4 - 1621977063431n^3 - 467241407430n^2 \\ & - 45622126368n)t^7 + \frac{1}{35012981203200000}(200810348470291303n^8 - 4171583882404341690n^7 \\ & + 8600742285944529613n^6 + 15634382372668953372n^5 - 3648271187242628015n^4 - 9801914187470665632n^3 \\ & - 3871241066318288229n^2 - 378804028118746050n + 39893821295328)t^8. \end{aligned} \quad (A2)$$

Correspondingly, the two-dimensional lattice system turns out to have the upper boundary

$$\begin{aligned} \mu_p = & n - 4(n+1)t - 2(3n^2 + 4n)t^2 - 4(11n^3 + 15n^2 + 4n)t^3 - \frac{1}{60}(10597n^4 + 24490n^3 + 17857n^2 + 4050n)t^4 \\ & - \frac{1}{450}(941863n^5 + 2188403n^4 + 1638443n^3 + 387253n^2 - 4650n)t^5 - \frac{1}{1512000}(17584506524n^6 \\ & + 56792815090n^5 + 70292096771n^4 + 41746636380n^3 + 12245886137n^2 + 1586224250n)t^6 - \frac{1}{952560000} \\ & (143621438541217n^7 + 482685930471859n^6 + 614916508856545n^5 + 357580517960125n^4 \\ & + 81552627354718n^3 - 3273334379504n^2 - 3097460700000n)t^7 - \frac{1}{17506490601600000} \\ & (15828728653296464701673n^8 + 66223539683880680581462n^7 + 114520168944419866201057n^6 \\ & + 106687922443046182561852n^5 + 59150401403670755097004n^4 + 20678487502333510720450n^3 \\ & + 4647036608792957074250n^2 + 556471872345686887500n)t^8, \end{aligned} \quad (A3)$$



and the lower boundary is determined by

$$\begin{aligned}
\mu_h = & n - 1 + 4nt + (6n^2 + 4n - 2)t^2 + 4n(n+1)(11n+7)t^3 + \frac{1}{60}(10597n^4 + 17898n^3 + 7969n^2 + 582n \\
& - 86)t^4 + \frac{1}{450}(941863n^5 + 2520912n^4 + 2303461n^3 + 816288n^2 + 91876n)t^5 + \frac{1}{1512000}(17584506524n^6 \\
& + 48714224054n^5 + 50095619181n^4 + 23183730284n^3 + 4598004583n^2 + 376989662n - 3186288)t^6 \\
& + \frac{1}{952560000}(143621438541217n^7 + 522664139316660n^6 + 734851135390948n^5 + 503463418187310n^4 \\
& + 173427383585083n^3 + 27374449536030n^2 + 1602049522752n)t^7 + \frac{1}{17506490601600000} \\
& (15828728653296464701673n^8 + 60406289542491037031922n^7 + 94159793449556113777667n^6 \\
& + 76147562446580745727476n^5 + 33700440149666544069539n^4 + 8032188219063211012704n^3 \\
& + 947361190459842328401n^2 + 50197343417953427898n - 85891426017677280)t^8. \tag{A4}
\end{aligned}$$

Finally, the upper boundary of a three-dimensional Mott lobe reads

$$\begin{aligned}
\mu_p = & n + (-6n - 6)t - 3(7n^2 + 8n)t^2 + (-231n^3 - 333n^2 - 102n)t^3 + \frac{1}{8}(-20683n^4 - 42646n^3 - 26919n^2 \\
& - 4990n)t^4 + \frac{1}{240}(-9450991n^5 - 23212861n^4 - 19367531n^3 - 6129431n^2 - 523770n)t^5 \\
& + \frac{1}{3024000}(-1612512639802n^6 - 4903150529490n^5 - 5568888652747n^4 - 2895859756680n^3 - 673691826835n^2 \\
& - 56132922750n)t^6 + \frac{1}{1270080000}(-11585180188993081n^7 - 40169594556544231n^6 - 54166855276590991n^5 \\
& - 35546615871621511n^4 - 11500224469294300n^3 - 1582089821730130n^2 - 46040315017500n)t^7 \\
& + \frac{1}{11670993734400000}(-1591704030486631948004941n^8 - 6411307825175115072269186n^7 \\
& - 10477219584627901596466499n^6 - 8903631755605628211005096n^5 - 4192954829256834761500718n^4 \\
& - 1081820439715328380764170n^3 - 143411169994732620393730n^2 - 8530598518867251187500n)t^8, \tag{A5}
\end{aligned}$$

where the low boundary is characterized by

$$\begin{aligned}
\mu_h = & (n - 1) + 6nt + 3(7n^2 + 6n - 1)t^2 + (231n^3 + 360n^2 + 129n)t^3 + \frac{1}{8}(20683n^4 + 40086n^3 + 23079n^2 \\
& + 3642n - 34)t^4 + \frac{1}{240}(9450991n^5 + 24042094n^4 + 21025997n^3 + 7205906n^2 + 771012n)t^5 + \frac{1}{3024000} \\
& (1612512639802n^6 + 4771925309322n^5 + 5240825602327n^4 + 2598442355448n^3 + 555628775407n^2 \\
& + 38549263230n - 50089536)t^6 + \frac{1}{1270080000}(11585180188993081n^7 + 40926666766407336n^6 \\
& + 56438071906180306n^5 + 38225048777927814n^4 + 13071729232591381n^3 + 2052306743024850n^2 \\
& + 109040959595232n)t^7 + \frac{1}{11670993734400000}(1591704030486631948004941n^8 \\
& + 6322324418717940511770342n^7 + 10165777662027790634720545n^6 + 8457647130735753938417688n^5 \\
& + 3856598073582426484397083n^4 + 937724839936122043372908n^3 + 107903564700275910537495n^2 \\
& + 4285936758470495239062n - 1004648837988860064)t^8. \tag{A6}
\end{aligned}$$

---

\* Corresponding author: [zxzf@physik.uni-kl.de](mailto:zxzf@physik.uni-kl.de)

<sup>1</sup> E. Dagotto. Rev. Mod. Phys. **66**, 763 (1994).

- <sup>2</sup> M. P. A. Fisher, P. B. Weichman, G. Grinstein, and D. S. Fisher. Phys. Rev. B **40**, 546 (1989).
- <sup>3</sup> D. Jaksch, C. Bruder, J. I. Cirac, C. W. Gardiner, and P. Zoller. Phys. Rev. Lett. **81**, 3108 (1998).
- <sup>4</sup> M. Greiner, O. Mandel, T. Esslinger, T. W. Hänsch, and I. Bloch. Nature (London) **415**, 39 (2002).
- <sup>5</sup> B. Yan, S. A. Moses, B. Gadway, J. P. Covey, K. R. A. Hazzard, A. M. Rey, D. S. Jin, and J. Ye. Nature (London) **501**, 521 (2013).
- <sup>6</sup> P. Schau, M. Cheneau, M. Endres, T. Fukuhara, S. Hild, A. Omran, T. Pohl, C. Gross, S. Kuhr, and I. Bloch. Nature (London) **491**, 87 (2012).
- <sup>7</sup> X.-F. Zhang, R. Dillenschneider, Y. Yu, and S. Eggert. Phys. Rev. B **84**, 174515 (2011).
- <sup>8</sup> D. Yamamoto, I. Danshita, and C. A. R. Sá de Melo. Phys. Rev. A **85**, 021601(R) (2012).
- <sup>9</sup> L. Bonnes and S. Wessel. Phys. Rev. B **84**, 054510 (2011).
- <sup>10</sup> X.-F. Zhang, Q. Sun, Y.-C. Wen, W.-M. Liu, S. Eggert, and A.-C. Ji. Phys. Rev. Lett. **110**, 090402 (2013).
- <sup>11</sup> X.-F. Zhang and S. Eggert. Phys. Rev. Lett. **111**, 147201 (2013).
- <sup>12</sup> J. K. Freericks and H. Monien. Phys. Rev. B **53**, 2691 (1996).
- <sup>13</sup> I. Hen, M. Iskin, and M. Rigol. Phys. Rev. B **81**, 064503 (2010).
- <sup>14</sup> M. Iskin. Phys. Rev. A **82**, 033630 (2010).
- <sup>15</sup> X.-F. Zhang, Y.-C. Wen, and Y. Yu. Phys. Rev. B **83**, 184513 (2011).
- <sup>16</sup> A. Eckardt. Phys. Rev. B **79**, 195131 (2009).
- <sup>17</sup> N. Teichmann, D. Hinrichs, M. Holthaus and A. Eckardt. Phys. Rev. B **79**, 224515 (2009).
- <sup>18</sup> T. Kato, Prog. Theor. Phys. **4**, 514 (1949).
- <sup>19</sup> F. E. A. dos Santos and A. Pelster. Phys. Rev. A **79**, 013614 (2009).
- <sup>20</sup> T. Wang, X.-F. Zhang, S. Eggert, and A. Pelster. Phys. Rev. A **87**, 063615 (2013).
- <sup>21</sup> F. Wei, J. Zhang, and Y. Jiang. Eur. Phys. Lett. **113**, 16004 (2016).
- <sup>22</sup> D. Hinrichs, A. Pelster, and M. Holthaus. Appl. Phys. B **113**, 57 (2013).
- <sup>23</sup> C. Heil and W. von der Linden. Phys. Rev. B **59**, 12184 (1999).
- <sup>24</sup> N. Elstner and H. Monien. J. Phys.: Condens. Matter **24**, 295601 (2012).
- <sup>25</sup> M. P. Gelfand and R. R. P. Singh. Advances in Physics **49**, 93 (2000).
- <sup>26</sup> T. D. Kühner and H. Monien. Phys. Rev. B **58**, 14741 (1998).
- <sup>27</sup> N. Elstner and H. Monien. Phys. Rev. B **59**, 12184 (1999).
- <sup>28</sup> S. Sachdev. *Quantum Phase Transitions*, 2nd edn. (Cambridge University Press, Cambridge, 2011).
- <sup>29</sup> J. Zinn-Justin. *Quantum field theory and critical phenomena*, 4th edn. (Oxford University Press, Oxford, 2002).
- <sup>30</sup> H. Kleinert and V. Schulte-Frohlinde. *Critical properties of  $\Phi^4$  theories* (World Scientific, Singapore, 2001).
- <sup>31</sup> B. Capogrosso-Sansone, S. G. Soyler, N. V. Prokofev, and B. Svistunov. Phys. Rev. A **77**, 015602 (2008).
- <sup>32</sup> B. Capogrosso-Sansone, N. V. Prokof'ev, and B. V. Svistunov. Phys. Rev. B **75**, 134302 (2007).
- <sup>33</sup> N. Teichmann and D. Hinrichs. Eur. Phys. J. B **71**, 219 (2009).
- <sup>34</sup> T. Wang, X.-F. Zhang, S. Eggert and A. Pelster. Phys. Rev. A **90**, 013633 (2014).
- <sup>35</sup> See Supplemental Material<sup>36</sup> for the Matlab code which calculates the high-order strong-coupling expansion for different filling in square lattice.
- <sup>36</sup> <http://power.itp.ac.cn/~zxf/source/HSCE.m>